# Nanoparticle enhanced anti-metastatic treatment of cancer with radiation

Yuting Qiu, Seng Kah Ng, Thomas Webster, Ming Su

Department of Chemical Engineering, Northeastern University, Boston, Massachusetts, 02115

Despite that over 90 percent of cancer deaths are due to metastasis formation, there is no anti-metastatic drug on the market. Ionizing radiation has shown capability in retarding tumor cell migration as a means to extend lifetime of patient, where high dose radiation needed may cause damage to normal tissue[1]. This article descries a new nanoparticle based method to enhance the anti-metastatic effect of ionizing radiation. Gold nanoparticles with large X-ray absorption cross section are modified, and incubated with prostate cancer cells[2]. The migration ability of cells is determined with migration tests, and cell viability is determined with a panel of techniques. The result indicates that nanoparticles can effectively prevent migration of cancer cells in the presence of radiation, compared with those with nanoparticle alone, and radiation alone[3-5].

Keywords: cancer cell migration, nanoparticles, X-ray radiation, anti-metastatic treatment.

## 1. Introduction

Cell migration is a complex multifaceted biological process that is regulated by an integrated network of biochemical and biomechanical events[6]. It involves the turnover of cell-substrate adhesion sites, the actin cytoskeleton that pulls the cells at the front, and the microtubule network responsible for cellular rear retraction in a coordinated sequence. From a biomechanical standpoint, cells will require active generation of traction force on the underlying extracellular matrix (ECM) to drive their forward motion[7]. Because of their size dimensions, it is hypothesized that endocytosed nanoparticles may interfere and interact at the molecular level with critical components of the cell migration machinery[8]. Cell migration is required for many biological processes, such as embryonic morphogenesis, immune surveillance, and tissue repair and regeneration. Aberrant regulation of cell migration drives progression of many diseases, including cancer invasion and metastasis. Cell migration is a highly integrated multistep process that is initiated by the protrusion of the cell membrane[7, 9, 10].

Despite extensive progress in glioblastoma multiforme (GBM) invasion in the last 30 years, the aggressive progress of the disease cause a median survival time of 15 months. The invasion process starts once tumor cells detach from their original site and invade the surrounding parenchymal cells and extracellular matrix (ECM)[11]. Cancer cell migration[12] is a critical step in tumor invasion, and motility of these cells has shown to directly relate to their metastatic potential. Several studies have reported that motile activity of tumor cells are guided by physical contact with underlying normal cells when invading surround tissues and forming metastases. cancer cell migration, invasion, and metastasis[13, 14]. Metastasis, the dissemination of cancer cells from the primary tumor to a distant organ, is the most frequent cause of death for patients with cancer. Cancer cell migration and invasion into adjacent tissues and intrava- sation into blood/lymphatic

vessels are required for metastasis of adenocarcinomas, the most common human cancers[15]. Invasive carcinoma cells acquire a migratory phenotype associated with increased expression of several genes involved in cell motility. This allows carcinoma cells to respond to cues from the microenvironment that trigger tumor invasion. Therefore, molecules involved in cancer cell migration could be potential targets for anti-metastasis therapy. Invasion of cancer cells into surrounding tissue and the vasculature is an initial step in tumor metastasis. This requires chemotactic migration of cancer cells, steered by protrusive activity of the cell membrane and its attachment to the extracellular matrix. Recent advances in intravital imaging and the development of an in vivo invasion assay have provided new insights into how cancer cell migration is regulated by elements of the local microenvironment, including the extracellular matrix architecture and other cell types found in primary tumors[16].

A challenge of radiation therapy is that therapeutic doses used can damage normal cells. The ions or nanoparticles of high atomic number elements (gold, platinum and bismuth) have been used to enhance radiation therapy by absorbing ionizing radiation and generating free radicals at high yield[17]. However, the measured enhancement effect of nanoparticles is negligible probably because nanoparticles are attached on cell membrane and X-ray generated free radicals are not in vicinity of DNA to cause damage to cancer cells. In particular, gold nanoparticles (GNPs) could be used as radio-sensitizers[18]. There is an urgent need to examine the effects of nanoparticles on cell migration as it is heavily implicated in cancer progression. Inhibition of cell migration after nanoparticle treatment has been reported. This article describes the first exploitation to use nanoparticle to suppress cancer cell migration with ionizing X-ray radiation[19].

## 2. Methods and Materials

### 2.1 Nanoparticle surface modification

Negative charged gold nanoparticles (5nm diameter) were obtained from Sigma, for modified gold nanoparticles, HAuCl4.3H2O stock solution was prepared by mixing 100 mg of AuCl4 in 5 ml of distilled water. then added 72 µl of 880 mM sodium borohydride (NaBH4) stock solution in deionized water over 30 min with stirring[20]. To make gold nanoparticles, 156 µL of 50.8 mM HAuCl4.3H2O stock solution and 169 µM of SH-PEG-COOH were dissolved in 25 ml of deionized water and stirred at room temperature for 1 hour. After adding NaBH4, the mixture was left for stirring for 3 hours. Extra SH-PEG-COOH and NaBH4 were added to ensure passivation of nanoparticles[21]. To make gold nanoparticles-PEG-CPP conjugates, PEG-COOH modified gold nanoparticles (2 mM) were mixed with CPP(WGRRVRRRIRRPPPPPPPPPGGK) at 400:1 (CPP/nanoparticle) ratio with 150 mM EDC and 7.5 mM sulfo-NHS (final concentration) in a 1 ml total reaction volume for 2 hours at room temperature[22].

2.2 Cell culture with surface modified gold nanoparticles

LN229 cell line was obtained from American Type Culture Collection (ATCC). We cultured cells in tissue culture flask (Thermo Scientific) in conventional incubator at 37 °C in an atmosphere of 5% $CO_2$ with DMEM medium (BioWhittaker) supplemented with 10% serum, 1% penicillin-streptomycin (Sigma-Aldrich) and 2mM glutamine (Life Technologies). Cells were seeded in 6-well plate at a concentration of 10^5 cells per well. After 24 hours, non-modified gold nanoparticles and CPP-PEG modified nanoparticles were incubated with cells at a final concentration of 10, 30, 50 µM and 10 µM respectively. Excess nanoparticles in the medium were removed after 24 hours incubation[23].

2.3 X-ray exposure

After 24 hours, Cells were irradiated with X-ray (40 kVp and 100 µA, 80 mGy/min) at the next day for 10 minutes respectively, and for 6-well plate with concentration of 10 µM, Cells

were irradiated with X-ray (40 kVp and 100 μA, 80 mGy/min) for 3mins, 8mins, 10mins 15 minutes respectively.

2.4 Cell migration assay

After the irradiation with with X-ray for certain time, scraped the cell monolayer in a straight line to create a ‘‘scratch’’ with a p200 pipet tip. Remove the debris and smooth the edge of the scratch by washing the cells once with 1 ml of the growth medium. It is important to create scratches of approximately similar size in the assessed cells and control cells to minimize any possible variation caused by the difference in the width of the scratches. To obtain the same field during the image acquisition, create markings to be used as reference points close to the scratch. The reference points can be made by etching the dish lightly with a razor blade on the outer bottom of the dish or with an ultrafine tip marker. After the reference points are made, place the dish under a phase-contrast microscope, and leave the reference mark outside the capture image field but within the eye-piece field of view. Acquire the first image of the scratch. Place the dish in a tissue culture incubator at 37.1C for 4–24h. The time frame for incubation should be determined empirically for the particular cell type used. The dishes can be taken out of the incubator to be examined periodically (4h one time) and then returned to resume incubation. Choose a time frame of incubation that allows the cells under the fastest migrating condition to just achieve the complete closure of the scratch. After the incubation, place the dish under a phase-contrast microscope, match the reference point, align the photographed region and acquire a second image. The images acquired for each sample can be further analyzed quantitatively by using computing software of choice (Matlab). For each image, distances between one side of scratch and the other can be measured at certain intervals (mm) using Matlab. This method will provide large sample sizes that are easily quantified statistically. Then measure the distance between the scratch.

2.5 Cell proliferation assay

Cells were grown in 96 well plates (Corning) and at approximately 70% cell confluence. Gold nanoparticles at various concentrations (10, 30, 50μM) were added in cell culture media in triplicates. Cells were irradiated with X-ray (40 kVp and 100 μA) at the next day for 10minutes. After 24hours, Vybrant MTT cell proliferation assay (Life Technologies) was performed. Absorbance was measured according to vendor instruction with SpectraMax M3 plate reader (Molecular Devices). Two independent sets of experiments were performed[24].

2.6 Reactive oxygen species (ROS) production

Carboxy-H2DCFDA was used to measure ROS production. In the presence of ROS, Carboxy-H2DCFDA is oxidized and emits green fluorescent. Carboxy-H2DCFDA was added at a final concentration of 1 μM into wells of 96 well microplates. Gold nanoparticles were added at a concentration of 10, 20, 30 and50μM a day prior to the experiment. The microplates were incubated for 30 minutes protected from light. The medium containing Carboxy-H2DCFDA was removed and washed twice with PBS. After adding fresh medium, cells were immediately irradiated with X-ray (40 kV 100 μA) for 10minutes, followed by incubation for one hour. The fluorescence intensity was measured using SpectraMax M3 fluorescence plate reader using 492nm excitation and 527nm emission wavelengths respectively[25].

2.6 DNA damage

Cells were incubated with gold nanoparticles on 6well culture dish which each well contained one sterilized coverslip, after 24h, cells were exposed to X-ray (40 kV 100 μA) for 10 minutes. After 24h, cells are mounted onto glass slide using mounting medium vetashield (Vector) containing DAPI (4',6-diamidino-2-phenylindole). DAPI is a fluorophore that can visualize nuclei content by binding strongly to adenine-thymine rich regions in DNA. Hence, if there are any

serious DNA damages, the change of nuclei morphology can be observed with DAPI staining[26]. The samples were visualized using confocal microscope (ZEISS), and more than 60 cells were counted to determine if their DNA were damaged.

2.7 Immunofluorescence staining

Cells are cultured on cover slips in 6 wells plates and exposed to X-ray (40 kV 100 μA) for 10 minutes. 24h after irradiation, the cells are fixed by 4% paraformaldehyde for 10 minutes, washed with washing buffer for three times and incubated with blocking buffer (1% BSA, and 0.2% Triton-X 100 in PBS) for 1 hour at room temperature. Primary antibodies for tubulin (Sigma1:2000) were incubated overnight at 4°C in blocking buffer. The next day, cover slips were washed three times in washing buffer, and mouse secondary antibody (In vitrogen, 1:2000) was added for 2 hours at room temperature. The cover slips were then rinsed three times in washing buffer before mounting on glass slides[27]. A confocal laser scanning microscope (Zeiss) with 20 X magnification was used to collect all images.

2.8 Differential interference contrast (DIC) microscope

Differential interference contrast (DIC) microscopy was used to determine the location of gold nanoparticles inside cells as follows. TPMT image setting on the Zen software was selected, and DIC III filtered with light polarizer was in place to get DIC effect. For Z-sectioning DIC images, maximum projections of 15 images of *z*-planes 1μm apart were taken and merged to one image. DIC images were taken with 60X magnification. All images were taken digitally processed with Adobe PhotoShop CC 2014 (Adobe Systems Inc., Mountain View, CA).

2.9 Apoptosis study

Cells treated with modified gold nanoparticles were stained with Annexin V–FITC and PI and evaluated for apoptosis by flow cytometry according to FITC Annexin V apoptosis detection

kit 1 manufacturer's protocol (BD PharMingen). Approximate 100,000 cells were washed twice with ice cold phosphate-buffered saline (PBS), and stained with 5 μl of Annexin V–FITC and 5 μl of PI in binding buffer (10 mM HEPES, pH 7.4, 140 mM NaOH, 2.5 mM CaCl) for 15 min at room temperature in the dark. Apoptotic cells were determined using a Becton-Dickinson FACScan cytoflurometer (Mansfield, MA, USA). Both early apoptotic (annexin V-positive, PI-negative) and late (annexin V-positive and PI-positive) apoptotic cells were included in cell death determinations.

**3. Results and Discussions**

3.1 Internalization of gold nanoparticles

Figure 1A showed that cell incubated with nanoparticles combined with radiation migrated slower than cells which incubated only with nanoparticles, cells which incubated with nanoparticles moved slower than untreated cells. Figure 1C showed that all cells incubated with gold nanoparticles contain vesicles internally, while most of cells have or contained these vesicles. Z-sectioning of sample was carried out to detect all the potential vesicles that are present in the cells, and the images were merged together using maximum projection setting. The maximum projection images (Figure 1C) clearly show that cells incubated with gold nanoparticles contained a large amount of nanoparticles inside cells. For untreated cells, there were no nanoparticles present intracellully might be vacuoles involved in normal metabolic activities (Figure 1B). Figure1D and 1E shows the 3D image of figure 1B and 1C.

3.2 Migration of cells incubated with positive charged gold nanoparticles

Figure 2A showed that cells incubated with positive charged gold nanoparticles and then were exposed to X-ray (40 kV 100 μA) for 10 minutes, figure 2B showed the scratch in each well covered with cells, after 4 scratch became smaller due to the migration of cells which showed in

figure 2C, eventually, the scratch were covered with cells showed in figure 2D. Positive NPs treatment (50μM) reduced cell sheet migration and increased cell traction of cells, cell migration index, which measures the difference between the width of the scratch at the onset and 12h post NPs treatment, normalized by its original scratch width, was introduced to quantify cell migration. A migration index of figure2E thus indicated at same dose of X-ray exposure, the groups with different NPs treatments had different cells' ability to close up the gap, compared to the untreated control, cells treated with the NPs(50μM) displayed significant decrease in the cells' ability to close up the gap in a dose-dependent manner[28]. Figure F showed that same concentration of nanoparticles with different doses of X-ray, 3.000GY treatment increased cell traction independent of cell migration[29]. Cells treated with more dose of X-ray resulted in more loss of intracellular filamentous microtubule network. As for normal cells(fibroblast), it showed little difference between groups treated with different concentration of NPs which showed in figure 2G.

3.3 Migration of cells incubated with different diameter of negative charged gold nanoparticles

Figure 3A,B,C,D shows the change of cells's morpholohy after being treated with 20 μM of negative charged gold nanoparticles with irradiation. The viabilities of cells treated with diameter of 5nm and 10nm negative charged gold nanoparticles were monitored with MTT assay which shows in figure 3E. Figure 3F and 3G shows that cells treated with different concentration of 10nm NPs while the other showed that cells treated with different doses of X-ray. Figure 3H shows that cells were treated with different concentration of 5nm NPs, and different doses of X-ray applied to cells with same concentration of 5nm NPs is showed in figure 3I.

3.4 Immunofluorescence upon X-ray irradiation

In embryogenesis, cellular migrations are a recurring theme in important morphogenic processes ranging from gastrulation to development of the nervous system. Migration remains

prominent in the adult organism, in normal physiology as well as pathology. Integrins relay molecular cues regarding the cellular environment that influence cell shape, survival, proliferation, gene transcription and migration. Following ligand binding, integrins cluster into focal contacts that contain many different actin-associated proteins, we observed α-tubulin, which link the integrin to the intracellularly, actomyosin-microtubules are in a tightly regulated dynamic balance. Contractility is generated as the actomyosin motor proteins slide along the tubulin filaments that are transmitted to the ECM via the focal adhesion proteins. Conversely, microtubules serve as compressional elements to counteract the contractility and this dynamic balance thus prevent catastrophic collapse of the cell structure[30]. Since NPs with radiation has recently been reported to have an affinity to microtubular proteins, Nanoparticles distribution is influenced by their ability to use cancerous cells features for own inactivation. Radiation therapy with ionizing radiations is employed extensively for treatment of cancer cells. We can observe have disrupted intracellular microtubules assembly leading to an increase in cell traction[31]. Figure 4A, 4B, 4C shows the shape of samples of control, same negative charged NPs concentration combined 0.75GY, 2.00GY X-ray. The shape of samples with same concentration of positive charged NPs with 0.75GY, 2.00GY, 3.00GY X-ray are showed in Figure 4E, 4F, 4G. The viabilities of cells treated with different concentration of negative charged NPs and positive charged modified gold nanoparticles were monitored with MTT assay. With X-ray irradiation, 45.1% of cells treated with combined negative charged NPs(50 μM) died a day later as compared to untreated cells as showed in Figure 4D(the dark grey one)[32]. The survival rates from other treatments ranged from 82 to 60%. Without irradiation, 33.7% of cells treated with negative charged NPs(50 μM) died as compared to the untreated cells as showed in Figure 4D(the light grey one). Survival rate from positive charged NPs treatments with irradiation(50 μM) was 48% as showed in 4H(the dark grey one). Taken

together, 50 μM of PEG-CPP modified positive charged gold nanoparticles exhibited a more cytotoxicity effect on LN229 cells after X-ray irradiation as compared to other gold nanoparticles modification(negative charged) which can significantly affect the migration of cells[33].

3.5 Flow cytometry

Extensive DNA damage can led to either apoptosis or cell death. Flow cytometry is used to determine if cell death caused by X-ray irradiation with PEG-CPP positive charged modified gold nanoparticles is mainly due to cells undergoing apoptosis or necrosis. Figure 5A and 5B shows that 20μM PEG-CPP modified gold nanoparticles were incubated with cells and irradiated with different doses of X-ray. The following day, the cells were analyzed using flow cytometry using annexin V/PI double staining. 32.84% of cell death was observed with 0.75GY as showed in Figure 5C. Out of these dying cells, 30 % were caused by early or late apoptosis (Figure 5D, light grey one). In contrast, 77% of radiated cells were dying, and 30 % of these cells died by apoptosis with 3.00GY which is showed in Figure 5D. Figure 5C indicates the viability of cells with different doses of X-ray. Hence, a larger number of cells died by necrosis when treated with larger dose of X-ray irradiation combined with PEG-CPP modified gold nanoparticles, which can result a slower migration of cells[34].

3.6 DNA damage upon X-ray irradiation

When there is insult to DNA integrity, H2AX protein level is up-regulated. High level of phosphorylation on Ser-140 of H2AX is linked to cell death after DNA damage. ROS induction is partly mediated by increasing H2AX level. So understanding the correlation of DNA damage with level of H2AX phosphorylation after X-ray irradiation is important to determine cell fate after DNA damage which can lead to leading to an increase in cell traction, X-ray irradiated cells

were stained with DAPI and images were taken using confocal microscope to determine the level of damage to DNA[35]. Figure 6D shows a larger number of nuclei of cells treated with PEG-CPP modified positive charged NPs(50 μM) appeared damaged with a distorted nuclei structure, compared to other treatment. To determine the proportion of damaged nuclei, at least 60 nuclei were counted from each group and the results were tabulated on Figure 6I. 28%, 30% and 42% of irradiated nuclei were severe, moderate and no damaged when treated with PEG-CPP modified gold nanoparticles(50 μM) combined X-ray, respectively, while In addition, Figure 6E to 6H shows that cells treated with negative charged NPs with same dose of X-ray, the nuclei of each sample, respectively. The percentage of damaged nuclei with different concentration of modified PEG-CPP positive NPs is showed in figure 6I, while figure 6J shows the percentage of damaged nuclei with different concentration of negative charged NPs. Hence, we know the percentage of severe damaged nuclei of positive charged sample is larger the negative charged one[36].

3.7 ROS production upon X-ray irradiation

Ionizing X-ray radiation causes water radiolysis, generating intracellular reactive oxygen species (ROS). ROS can cause oxidation damage to DNA, resulting in single or double DNA strand breakage and giving rise to genomic instability. To determine if PEG-CPP modified positive charged gold nanoparticles can enhance ROS production after X-ray irradiation (40 kV and 100 mA), cells were incubated overnight with NPs. An approximate significant increase in ROS production was observed when cells treated with PEG-CPP positive charged modified gold nanoparticles were exposed to X-ray radiation, as compared to negative charged NPs treated cells as showed in figure 6K and 6L. Hence, a larger concentration of PEG-CPP modified gold nanoparticles could more significantly enhance ROS production after irradiation when they were internalized in the cells as showed both in 6K and 6L[37].

## 4. Conclusions

PEG-CPP modified positive charged gold nanoparticles were more effective in retarding migration of cells after X-ray irradiation when compared to negative charged gold nanoparticles. One reason might be that PEG-CPP modified gold nanoparticles can generate more reactive oxygen species within LN229 cells after X-ray irradiation[38]. The type and binding kinetics of the adsorbed protein on the NP surface were expected to govern intracellular interaction and exert considerable biological impacts on the cells[39]. Taken together, the evidence showed that the influence of NPs on cellular migration was acting through some machinery that is within the cell and not merely due to the NP-induced acute cytotoxicity[40-42]. PEG-CPP modified gold nanoparticles have the potential to damage cells nuclei by enhancing free radical generation[43, 44].

## 5. Acknowledgement

This project was supported by a NIH Director's New Innovator Award(1DP2EB016572).

## Figure Captions

Figure 1. Suppressing Migration of Brain Cancer Cells using penetrating peptide modified gold nanoparticles (A) positive charged NPs treatment increases cell traction and retards collective cell sheet migration of LN229 cells. (B) 2D formation of untreated cells. (C) 2D of Z- sectioning at 1 μM thickness merged using maximum projection function cells with nanoparticles. (D) 3D formation of untreated cells. (E) 3D of Z- sectioning at 1 μM thickness merged using maximum projection function cells with nanoparticles. Scale bar is 10 μm.

Figure 2. (A) Analysis of LN229 cells migration by scratch assay at 0h. (B), (C) and (D) Measurement of individual cell migration in scratch assay. Scratch assay with images captured at 4, 8 and 20h after incubation using fluorescence or phase-contrast microscope. Scale bar = 20 μm. The rate of migration was measured by quantifying the total distance that LN229 cells (as indicated

by arrows) moved from the edge of the scratch toward the center of the scratch. (E) positive charged different concentration of NPs treatment (0-50μM) with same dose X-ray (40 kVp and 100 μA, 80 mGy/min) reduced cell sheet migration and increased cell traction of cells at leading edge. (F) positive charged NPs(20 μM) treatment with different dose X-ray(40 kVp and 100 μA, 80 mGy/min), 3.00GY has significantly delayed onset of cell migration and cell sheet displacement. (G) fibroblast cells treated with positive charged different concentration of NPs treatment (0-50μM) with same dose X-ray (40 kVp and 100 μA, 80 mGy/min), there is no significant difference among each sample. Error bars in (E,F,G) represent standard deviation of the means from three independent experiments. * denotes statistical significance between the untreated control versus NPs treated samples.$p < 0.05$, Student's t test.

Figure 3. (A) (B) (C) (D) shows the change of cells's morpholohy after being treated with 20 μM of negative charged gold nanoparticles with irradiation.(0h, 4h, 8h, 12h), Scale bar = 20 μm. (E) Cytotoxicity of negative charged gold nanoparticles with diameter of 5nm with X-ray and no X-ray and 10nm with X-ray and no X-ray. (F) LN229 cells treated with different concentration (0-50μM) of negative charged gold nanoparticles with diameter of 10nm combined same dose of X-ray. (G) LN229 cells treated with different doses of X-ray with same concentration of diameter of 10nm negative charged NPs. (H) cells treated witn PEG-CPP modified positive charged gold nanoparticles with same dose of X-ray. (I) cells treated with same concentration modified positive charged NPs with different doses of radiation, which resulted in the loss of intracellular filamentous microtubule network. NPs treatment destabilizes microtubule network and induces global cytoskeletal and focal adhesion remodeling resulted in the loss of intracellular filamentous microtubule network. Error bars in (E,F,G,H,I) represent standard deviation of the means from three independent experiments. * denotes statistical significance between the untreated control

versus NPs treated samples. $p < 0.05$, Student's t test.

Figure 4. (A) the shape of sample with no X-ray, same negative charged NPs concentration(30 μM) combined 0.75GY(B), 2.00GY(C) dose of radiation. Scale bar = 20 μm. The shape of samples with same concentration of positive charged NPs with 0.75GY(E), 2.00GY(F), 3.00GY(G) dose of radiation, (G) lowered expression level of stabilized tubulin network (acetylated α-tubulin) in the cells which induced an increased actin remodelling and focal adhesions formation. (D) the percentage of cell proliferation after being treated with different concentration of negative charged NPs combined 2.00GY dose of radiation. (H) the percentage of cell proliferation after being treated with different concentration of PEG-CPP modified positive charged NPs combined 2.00GY dose of radiation. Error bars in (D,H) represent standard deviation of the means from three independent experiments. * denotes statistical significance between the untreated control versus NPs treated samples.$p < 0.05$, Student's t test.

Figure 5. PEG-CPP modified gold positive nanoparticles treated cells with (B) and without (A) X-ray irradiated. (C) The percentage of cells viability after being enhanced apoptosis in X-ray exposed with CPP-PEG modified gold nanoparticles. (D) Cells were scored for annexin V/PI double staining to determine the relative amount of live cells, apoptotic cells (light grey), necrotic cells (dark grey) cells (top right), respectively. Error bars in (C) represent standard deviation of the means from three independent experiments. * denotes statistical significance between the untreated control versus NPs treated samples.$p < 0.05$, Student's t test.

Figure 6. Reactive oxygen species (ROS) production after X-ray irradiation. Fluorescence images showing levels of nuclei when cells treated with PEG-CPP positive charged nanoparticles with no X-ray(A), 0.75GY(B), 2.00GY(C) and 3.00GY(D) of X-ray irradiation, cells treated with negative

charged nanoparticles with no X-ray(E), 0.75GY(F), 2.00GY(G) and 3.00GY(H) of X-ray irradiation. Scale bar = 10μm, The percentage of DNA damage level after treated with positive charged NPs(I), treated with negative charged NPs(J), (Light grey bar: No DNA damage, Grey bar: Moderate DNA damage, Dark grey bar: Severe DNA damage). The amount of ROS produced using carboxy-H2DCFDA assay shows when cells were treated with different concentration of PEG-CPP modified gold nanoparticles (K) and negative charged nanoparticles (L) underwent and no X-ray irradiation, (dark grey with X-ray, light grey no-X-ray). Error bars in (K,L) represent standard deviation of the means from three independent experiments. * denotes statistical significance between the untreated control versus NPs treated samples. $p < 0.05$, Student's t test.

**References**


1. Raftopoulou, M. and A. Hall, Cell migration: Rho GTPases lead the way. Developmental Biology, 2004. 265(1): p. 23-32.
2. Watanabe, T., J. Noritake, and K. Kaibuchi, Regulation of microtubules in cell migration. Trends Cell Biol, 2005. 15(2): p. 76-83.
3. Decaestecker, C., et al., Can anti-migratory drugs be screened in vitro? A review of 2D and 3D assays for the quantitative analysis of cell migration. Med Res Rev, 2007. 27(2): p. 149-76.
4. Liang, C.C., A.Y. Park, and J.L. Guan, In vitro scratch assay: a convenient and inexpensive method for analysis of cell migration in vitro. Nat Protoc, 2007. 2(2): p. 329-33.
5. Murphy, C.J., et al., Gold nanoparticles in biology: beyond toxicity to cellular imaging. Acc Chem Res, 2008. 41(12): p. 1721-30.
6. Tay, C.Y., et al., Nanoparticles strengthen intracellular tension and retard cellular migration. Nano Lett, 2014. 14(1): p. 83-8.
7. Qiao, Y., et al., Reducing X-Ray Induced Oxidative Damages in Fibroblasts with Graphene Oxide. Nanomaterials (Basel), 2014. 4(2): p. 522-534.
8. Zhang, P., et al., Enhanced radiation therapy with internalized polyelectrolyte modified nanoparticles. Nanoscale, 2014. 6(17): p. 10095-9.
9. Dykman, L.A. and N.G. Khlebtsov, Uptake of engineered gold nanoparticles into mammalian cells. Chem Rev, 2014. 114(2): p. 1258-88.
10. Hong, Y., et al., Molecular recognition of proteolytic activity in metastatic cancer cells using fluorogenic gold nanoprobes. Biosens Bioelectron, 2014. 57: p. 171-8.
11. Matea, C.T., et al., Rational design of gold nanocarrier for the delivery of JAG-1 peptide. J Nanobiotechnology, 2015. 13: p. 41.

12. Jen, C.P., et al., A nonviral transfection approach in vitro: the design of a gold nanoparticle vector joint with microelectromechanical systems. Langmuir, 2004. 20(4): p. 1369-74.
13. Cao, G., et al., Generation of gold nanostructures at the surface of platinum electrode by electrodeposition for ECL detection for CE. Electrophoresis, 2010. 31(6): p. 1055-62.
14. Hainfeld, J.F., et al., Gold nanoparticles enhance the radiation therapy of a murine squamous cell carcinoma. Phys Med Biol, 2010. 55(11): p. 3045-59.
15. Rahman, W.N., et al., Enhancement of radiation effects by gold nanoparticles for superficial radiation therapy. Nanomedicine: Nanotechnology, Biology and Medicine, 2009. 5(2): p. 136-142.
16. Comfort, K.K., et al., Interference of silver, gold, and iron oxide nanoparticles on epidermal growth factor signal transduction in epithelial cells. ACS Nano, 2011. 5(12): p. 10000-8.
17. Kim, J.H., et al., The inhibition of retinal neovascularization by gold nanoparticles via suppression of VEGFR-2 activation. Biomaterials, 2011. 32(7): p. 1865-71.
18. Mesbahi, A., A review on gold nanoparticles radiosensitization effect in radiation therapy of cancer. Rep Pract Oncol Radiother, 2010. 15(6): p. 176-80.
19. Brun, E., et al., Gold nanoparticles enhance the X-ray-induced degradation of human centrin 2 protein. Radiation Physics and Chemistry, 2009. 78(3): p. 177-183.
20. Fukata, M., M. Nakagawa, and K. Kaibuchi, Roles of Rho-family GTPases in cell polarisation and directional migration. Current Opinion in Cell Biology, 2003. 15(5): p. 590-597.
21. Hainfeld, J.F., D.N. Slatkin, and H.M. Smilowitz, The use of gold nanoparticles to enhance radiotherapy in mice. Physics in Medicine and Biology, 2004. 49(18): p. N309-N315.
22. Condeelis, J. and J.W. Pollard, Macrophages: obligate partners for tumor cell migration, invasion, and metastasis. Cell, 2006. 124(2): p. 263-6.
23. Kessenbrock, K., V. Plaks, and Z. Werb, Matrix metalloproteinases: regulators of the tumor microenvironment. Cell, 2010. 141(1): p. 52-67.
24. Qian, B.Z. and J.W. Pollard, Macrophage diversity enhances tumor progression and metastasis. Cell, 2010. 141(1): p. 39-51.
25. Sperling, R.A. and W.J. Parak, Surface modification, functionalization and bioconjugation of colloidal inorganic nanoparticles. Philos Trans A Math Phys Eng Sci, 2010. 368(1915): p. 1333-83.
26. McMahon, S.J., et al., Nanodosimetric effects of gold nanoparticles in megavoltage radiation therapy. Radiother Oncol, 2011. 100(3): p. 412-6.
27. Menk, R.H., et al., Gold nanoparticle labeling of cells is a sensitive method to investigate cell distribution and migration in animal models of human disease. Nanomedicine, 2011. 7(5): p. 647-54.
28. Misawa, M. and J. Takahashi, Generation of reactive oxygen species induced by gold nanoparticles under x-ray and UV Irradiations. Nanomedicine, 2011. 7(5): p. 604-14.
29. Aziz, M.S., et al., Gold nanoparticle trapping and delivery for therapeutic applications. Int J Nanomedicine, 2012. 7: p. 11-7.
30. Jain, S., D.G. Hirst, and J.M. O'Sullivan, Gold nanoparticles as novel agents for cancer therapy. Br J Radiol, 2012. 85(1010): p. 101-13.
31. Kamaly, N., et al., Targeted polymeric therapeutic nanoparticles: design, development and clinical translation. Chem Soc Rev, 2012. 41(7): p. 2971-3010.
32. Zhang, X.D., et al., Size-dependent radiosensitization of PEG-coated gold nanoparticles for cancer radiation therapy. Biomaterials, 2012. 33(27): p. 6408-19.

33. Bhowmik, T., et al., Antileukemic potential of PEGylated gold nanoparticle conjugated with protein toxin (NKCT1) isolated from Indian cobra () venom. Cancer Nanotechnol, 2013. 4(1-3): p. 39-55.
34. Fearon, A.E., C.R. Gould, and R.P. Grose, FGFR signalling in women's cancers. Int J Biochem Cell Biol, 2013. 45(12): p. 2832-42.
35. Gromnicova, R., et al., Glucose-coated gold nanoparticles transfer across human brain endothelium and enter astrocytes in vitro. PLoS One, 2013. 8(12): p. e81043.
36. Joh, D.Y., et al., Theranostic Gold Nanoparticles Modified for Durable Systemic Circulation Effectively and Safely Enhance the Radiation Therapy of Human Sarcoma Cells and Tumors. Translational Oncology, 2013. 6(6): p. 722-IN32.
37. Kumari, S. and R.P. Singh, Glycolic acid functionalized chitosan-Au-Fe(3)O(4) hybrid nanoparticle based nanohybrid scaffold for drug delivery. Int J Biol Macromol, 2013. 54: p. 244-9.
38. Yang, J.A., et al., Nanovacuums: nanoparticle uptake and differential cellular migration on a carpet of nanoparticles. Nano Lett, 2013. 13(5): p. 2295-302.
39. Betzer, O., et al., Nanoparticle-based CT imaging technique for longitudinal and quantitative stem cell tracking within the brain: application in neuropsychiatric disorders. ACS Nano, 2014. 8(9): p. 9274-85.
40. Rosman, C., et al., Mammalian cell growth on gold nanoparticle-decorated substrates is influenced by the nanoparticle coating. Beilstein J Nanotechnol, 2014. 5: p. 2479-88.
41. Skopalik, J., et al., Mesenchymal stromal cell labeling by new uncoated superparamagnetic maghemite nanoparticles in comparison with commercial Resovist--an initial in vitro study. Int J Nanomedicine, 2014. 9: p. 5355-72.
42. Sutradhar, K.B. and M.L. Amin, Nanotechnology in Cancer Drug Delivery and Selective Targeting. ISRN Nanotechnology, 2014. 2014: p. 1-12.
43. Yuan, Y., et al., Tumor-responsive fluorescent light-up probe based on a gold nanoparticle/conjugated polyelectrolyte hybrid. Small, 2014. 10(10): p. 1967-75.
44. Lin, C.M., et al., Hyaluronic acid-fabricated nanogold delivery of the inhibitor of apoptosis protein-2 siRNAs inhibits benzo[a]pyrene-induced oncogenic properties of lung cancer A549 cells. Nanotechnology, 2015. 26(10): p. 105101.

## Biomimetic 3D Clusters Using Cancer Cells: A Study on Migration and Invasion of Cancer Cells

Yuting Qiu[1], Liyuan Ma[1,2]*, Ming Su[1,2]*

[1]Department of Chemical Engineering, Northeastern University, Boston, MA 02115; [2]Wenzhou Institute of Biomaterials and Engineering, Wenzhou Medical University, Chinese Academy of Science, Zhejiang 325001;

Abstract: The need for more complete and physiologically predictive cancer growth and invasion

models has driven the development of the 3D Spheroid Assays. There is growing evidence that tumor cell aggregates or spheroids are more representative of tumors in vivo, and they exhibit several physiological traits including similar morphology, the formation of cell-cell bonds, decreased proliferation rates, increased cell survival, tumor dormancy, and a hypoxic core. Applying this model to 3D culture proliferation and invasion assays provides a more physiological approach for assessing tumor growth and invasion. Invasion and metastasis of cancer directly related to human death have been associated with interactions among many different types of cells and three-dimensional (3D) tissue matrices. Precise mechanisms related to cancer invasion and metastasis still remain unknown due to their complexities. Development of tumor microenvironment (TME)-mimicking system could play a key role in understanding cancer environments and in elucidating the relating phenomena and their driving forces. Here we report a facile and novel platform of 3D cancer cell-clusters using human adipose-derived mesenchymal stem cells (hASCs) and breast cancer cells (MDA-MB-231) within a collagen gel matrix to show cancer invasion in the cell and extracellular matrix (ECM). Both clusters A (hASC only) and AC (hASC and MDA-MB-231) exhibited different behaviors and expressions of migration and invasion, as observed by the relating markers such as fibronectin, α-SMA, and CXCR4. hASCs showed a protrusive migration from a cluster center, whereas MDA-MB-231 spread out radially followed by hASC migration. Finally, the effect of matrix was further discussed by varying collagen gel densities. The new biomimetic system of 3D cancer clusters developed here has the potential to be utilized for research on migration and invasion of cancer cells in extracellular matrices. advances in cancer research have shown that a tumor can be likened to a foreign species that disrupts delicately balanced ecological interactions, compromising the survival of normal tissue ecosystems. In efforts to mitigate tumor expansion and metastasis, experimental approaches

from ecology are becoming more frequently and successfully applied by researchers from diverse disciplines to reverse engineer and re-engineer biological systems in order to normalize the tumor ecosystem. We present a review on the use of 3D biomimetic platforms to recapitulate biotic and abiotic components of the tumor ecosystem, in efforts to delineate the underlying mechanisms that drive evolution of tumor heterogeneity, tumor dissemination, and acquisition of drug resistance. As tumors proliferate, their energy and oxygen requirements o en cannot be met by existing tissue vasculature. Hypoxia is also associated with drug resistance as low oxygen tensions a ect the cell cycle and slow cycling cells are thought to be minimally a ected by treatments targeting the cell cycle. It has also been implicated in upregulation of genes that regulate cell proliferation, ECM production, cell adhesion, and cell invasion through induction of the hypoxia-inducible factor (HIF) family of transcription factors. Neoangiogenesis in part alleviates growth-induced hypoxia but tumor vasculature lacks the normal hierarchical arrangement of artery–arteriole–capillary, resulting in intercellular gaps that leak uids, blood, and brins, and inefficient oxygen delivery. Consequently, within the growing mass, there are regions of hypoxia where certain cancer cells are deprived of oxygen. In response, tumor cells may undergo a metabolic shi causing acidosis. Hydrogen ($H^+$) ions generated by tumor cells during both aerobic and anaerobic glycolysis, glutaminolysis, and ATP hydrolysis are transported to the extracellular milieu creating an acidic tumor microenvironment. ese acidic environments are thought to be permissive for tumor invasion and successive metastasis by inducing cell death in the surrounding normal tissue and degradation of the ECM. Three-dimensional (3D) culture systems in which extracellular matrices that biochemically and physically mimic the *in vivo* composition of

organs have been extensively used to study normal epithelial organogenesis for the breast, prostate, salivary gland, and kidney. In addition, pharmaceutical studies involving endothelial cell-derived 3D spheroids have been extensively used for evaluating the pro and anti-angiogenic potential of drugs targeting the tumor vasculature. In these biomimetic systems, cells adopt physiological morphologies and the appropriate cell signaling is achieved. 3D culture models can also be used to recapitulate the abiotic and biotic components of the tumor ecosystem. Namely, the abiotic components such as the spatiotemporal gradients of chemicals, oxygen tension, and mechanical cues can be robustly engineered using applications from microuidics, electrospinning, and so lithography. e biotic components such as the ECM environment and heterotypic cell interactions can also be approximated using biomimetic platforms and co- culture systems. Although the conventional two-dimensional (2D) tissue culture system has contributed enormously to the progress of cancer biology, cancer cells encounter diverse 3D topographies and architectures in vivo. us, 3D culture models allow for deconstructing the complexity of cancer by recapitulating emergent, population-level characteristics of the tumor microenvironment. Cellular microenvironment of a tumor is characterized by cells and biochemical components and by their complex interactions with the physical and chemical parameters such as stiffness, pH, oxygen tension, interstitial pressure. Both tumor and stromal cells create gradients of secreted cytokines and growth factors, which contribute to altered proliferation and directed cell migration to facilitate tumor progression, dissemination, and invasion.

An emerging and exciting field for bioprinting applications could be immunotherapy approaches in cancer, which are designed to boost immune defenses to fight tumors. These approaches are to either: (i) use biologics, such as antibodies and antibody-recruiting molecules to enhance the immune response, or (ii) engineer a patient's cytotoxic T cells with chimeric antigen recep- tors (CARs), then transfer the cells back to the patient to seek and destroy their tumors. Both of these approaches have shown remarkable success in clinical trials, in some cases resulting in a completely curing cancer that had become resistant to all available treatment options. However, not all patients with the same tumor types respond to immunotherapy approaches. In many solid tissue tumors, there is also the challenge of generating cytotoxic T cells to migrate or infiltrate into the tumor sites and determining how tumor cells evade these cells. In both of these challenges, 3D bioprinting of tumors would provide excellent models to study mechanistic interactions between the immune and tumor cells, testing novel biologics, drugs, or engineered T cells with novel synthetic targeting/activating molecules to develop the next generation of immunotherapy treatments. It is also conceivable that, to identify ideal personalized treatment options for a particular patient, robust bioprinting approaches may fabricate patient-derived tumors to test therapies with their own natural or engineered immune cells.

The microenvironment：Cell morphology (structure,phenotype)，Polarity(functionaldirectionality)，Growth(proliferation)，Cellmotility(migration,invasion)，Neuriteoutgrowth，Signal transduction (surface receptor function)，Gene and protein expression (different cell types can express different genes/proteins; liver vs. heart vs. brain)，Biochemicalactivities(proteins,enzymes).

Addition: Three-dimensional (3D) culture systems in which extracellular matrices that biochemically and physically mimic the in vivo composition of organs have been extensively used to study normal epithelial organogenesis for the breast, prostate, salivary gland, and kidney. In addition, pharmaceutical studies involving endothelial cell-derived 3D spheroids have been extensively used for evaluating the pro and anti-angiogenic potential of drugs targeting the tumor vasculature. In these biomimetic systems, cells adopt physiological morphologies and the appropriate cell signaling is achieved. 3D culture models can also be used to recapitulate the abiotic and biotic components of the tumor ecosystem. Namely, the abiotic components such as the spatiotemporal gradients of chemicals, oxygen tension, and mechanical cues can be robustly engineered using applications from microuidics, electrospinning, and so lithography. e biotic components such as the ECM environment and heterotypic cell interactions can also be approximated using biomimetic platforms and co- culture systems. Although the conventional two-dimensional (2D) tissue culture system has contributed enormously to the progress of cancer biology, cancer cells encounter diverse 3D topographies and architectures in vivo. us, 3D culture models allow for deconstructing the complexity of cancer by recapitulating emergent, population-level characteristics of the tumor microenvironment. Cellular microenvironment of a tumor is characterized by cells and biochemical components and by their complex interactions with the physical and chemical parameters such as stiffness, pH, oxygen tension, interstitial pressure. Both tumor and stromal cells create gradients of secreted cytokines and growth factors, which contribute

to altered proliferation and directed cell migration to facilitate tumor progression, dissemination, and invasion.

As tumors proliferate, their energy and oxygen requirements cannot be met by existing tissue vasculature. Hypoxia is also associated with drug resistance as low oxygen tensions affect the cell cycle and slow cycling cells are thought to be minimally affected by treatments targeting the cell cycle. It has also been implicated in upregulation of genes that regulate cell proliferation, ECM production, cell adhesion, and cell invasion through induction of the hypoxia-inducible factor (HIF) family of transcription factors. Neoangiogenesis in part alleviates growth-induced hypoxia but tumor vasculature lacks the normal hierarchical arrangement of artery–arteriole–capillary, resulting in intercellular gaps that leak, blood, and brains, and inefficient oxygen delivery. Consequently, within the growing mass, there are regions of hypoxia where certain cancer cells are deprived of oxygen. In response, tumor cells may undergo a metabolic shi causing acidosis. Hydrogen (H+) ions generated by tumor cells during both aerobic and anaerobic glycolysis, glutaminolysis, and ATP hydrolysis are transported to the extracellular milieu  creating an acidic tumor microenvironment. These acidic environments are thought to be permissive for tumor invasion and successive metastasis by inducing cell death in the surrounding normal tissue and degradation of the ECM.

Cancer is a complex disease in which the cancer cell population dynamically evolves and the diversity of heterotypic interactions between cancer cells, surrounding cells, and environmental factors is spatiotemporally regulated. Therefore, preclinical models that incorporate factors that play critical roles in the dynamic tumor progression, within a biomimetic landscape are needed. Three-dimensional culture models help to deconstruct the complexity of cancer. Model systems can be engineered to recapitulate tumor cell- surrounding cell interactions, the physicochemical

characteristics in an abiotic tumor environment, and the malignant transitions in tumor progression. They can provide insight into the evolutionary and ecological aspects of tumor progression, with relevant therapeutic implications.

Despite their great benefits over 2D models, 3D tissue models still encounter several limitations. One of their limitations lies in the requirement of large numbers of cells and cell types integrated into complex configurations. Second, ECM-derived matrices may have batch-to- batch variability in their biological characteristics. Some studies using standardized micro- fluidics- or microarray-based HTS for drug discovery or toxicity testing reported that specific ECM components or natural scaffolds were often not consistent. Third, 3D culture is generally very expensive for large-scale studies and high-throughput assays. Fourth, vascularization in 3D models remains an unsolved problem but it is the subject of active research, which plays a vital role in tissue growth and survival, and drug delivery. The core of tissue spheroids may create a hypoxic environment or limit the diffusion of compounds into the core. These shortcomings are mainly due to a low level of biomimetic organization of the heterocellular environment, and instability and low repeatability of the developed 3D models. Biomimetically developed miniaturized tissue models that meet these limitations, by contrast, may be fabricated by the accurate deposition of cells and ECM components to recapitulate the native architecture of tissues, which is highly feasible using 3D bioprinting. Examples to specific capabilities of bioprinting will be further discussed in the next section. hy 3D?' Such sessions are a thing of the past now because there is an accumulating body of evidence - joined by the recent article from Leslie and colleagues - demonstrating the importance and utility of 3D culture systems to discover and model biological process with in vivo relevance.

Three-dimensional (3D) culture systems in which extracellular matrices that biochemically and

physically mimic the in vivo composition of organs have been extensively used to study normal epithelial organogenesis for the breast, prostate, salivary gland, and kidney. In addition, pharmaceutical studies involving endothelial cell-derived 3D spheroids have been extensively used for evaluating the pro and anti-angiogenic potential of drugs targeting the tumor vasculature. In these biomimetic systems, cells adopt physiological morphologies and the appropriate cell signaling is achieved. 3D culture models can also be used to recapitulate the abiotic and biotic components of the tumor ecosystem. Namely, the abiotic components such as the spatiotemporal gradients of chemicals, oxygen tension, and mechanical cues can be robustly engineered using applications from microuidics, electrospinning, and so lithography. e biotic components such as the ECM environment and heterotypic cell interactions can also be approximated using biomimetic platforms and co- culture systems. Although the conventional two-dimensional (2D) tissue culture system has contributed enormously to the progress of cancer biology, cancer cells encounter diverse 3D topographies and architectures in vivo. us, 3D culture models allow for deconstructing the complexity of cancer by recapitulating emergent, population-level characteristics of the tumor microenvironment. Cellular microenvironment of a tumor is characterized by cells and biochemical components and by their complex interactions with the physical and chemical parameters such as stiffness, pH, oxygen tension, interstitial pressure. Both tumor and stromal cells create gradients of secreted cytokines and growth factors, which contribute to altered proliferation and directed cell migration to facilitate tumor progression, dissemination, and invasion.

As tumors proliferate, their energy and oxygen requirements cannot be met by existing tissue vasculature. Hypoxia is also associated with drug resistance as low oxygen tensions affect the cell cycle and slow cycling cells are thought to be minimally affected by treatments targeting the cell cycle. It has also been implicated in upregulation of genes that regulate cell proliferation, ECM

production, cell adhesion, and cell invasion through induction of the hypoxia-inducible factor (HIF) family of transcription factors. Neoangiogenesis in part alleviates growth-induced hypoxia but tumor vasculature lacks the normal hierarchical arrangement of artery–arteriole–capillary, resulting in intercellular gaps that leak, blood, and brains, and inefficient oxygen delivery. Consequently, within the growing mass, there are regions of hypoxia where certain cancer cells are deprived of oxygen. In response, tumor cells may undergo a metabolic shi causing acidosis. Hydrogen (H+) ions generated by tumor cells during both aerobic and anaerobic glycolysis, glutaminolysis, and ATP hydrolysis are transported to the extracellular milieu creating an acidic tumor microenvironment. These acidic environments are thought to be permissive for tumor invasion and successive metastasis by inducing cell death in the surrounding normal tissue and degradation of the ECM.

Cancer is a complex disease in which the cancer cell population dynamically evolves and the diversity of heterotypic interactions between cancer cells, surrounding cells, and environmental factors is spatiotemporally regulated. Therefore, preclinical models that incorporate factors that play critical roles in the dynamic tumor progression, within a biomimetic landscape are needed. Three-dimensional culture models help to deconstruct the complexity of cancer. Model systems can be engineered to recapitulate tumor cell- surrounding cell interactions, the physicochemical characteristics in an abiotic tumor environment, and the malignant transitions in tumor progression. They can provide insight into the evolutionary and ecological aspects of tumor progression, with relevant therapeutic implications.

Despite their great benefits over 2D models, 3D tissue models still encounter several limitations. One of their limitations lies in the requirement of large numbers of cells and cell types integrated into complex configurations. Second, ECM-derived matrices may have batch-to- batch variability

in their biological characteristics. Some studies using standardized micro- fluidics- or microarray-based HTS for drug discovery or toxicity testing reported that specific ECM components or natural scaffolds were often not consistent. Third, 3D culture is generally very expensive for large-scale studies and high-throughput assays. Fourth, vascularization in 3D models remains an unsolved problem but it is the subject of active research, which plays a vital role in tissue growth and survival, and drug delivery. The core of tissue spheroids may create a hypoxic environment or limit the diffusion of compounds into the core. These shortcomings are mainly due to a low level of biomimetic organization of the heterocellular environment, and instability and low repeatability of the developed 3D models. Biomimetically developed miniaturized tissue models that meet these limitations, by contrast, may be fabricated by the accurate deposition of cells and ECM components to recapitulate the native architecture of tissues, which is highly feasible using 3D bioprinting. Examples to specific capabilities of bioprinting will be further discussed in the next section.

The growth substrate is different, for 2D cell monolayer, it is rigid and insert, while 3D microtissues can mimic natural tissue environment. For, architecture, 2D cell monolayer is not physiological and cells partially interact while 3D structure is 'physiological', it can promote close interactions between cells and they have extracellular matrix(ECMs) as well as growth factors. There is no cell encapsulation in 2D cell monolayer. As for 2D cell monolayer, the growth factor diffusion is rapid, but for 3D microtissues, it is slow and biochemical gradients regulate cell-cell communication and signaling. ECM-based growth substrates provide a physiological environment that supports and promotes key cell functions, ECM molecules interact with cell surface receptors (e.g., regulation of integrin signaling by fibronectin: integrin interactions), also ECM appears to function in the storage and presentation of growth factors.

As tumors proliferate, their energy and oxygen requirements cannot be met by existing tissue vasculature. Hypoxia is also associated with drug resistance as low oxygen tensions affect the cell cycle and slow cycling cells are thought to be minimally affected by treatments targeting the cell cycle. It has also been implicated in upregulation of genes that regulate cell proliferation, ECM production, cell adhesion, and cell invasion through induction of the hypoxia-inducible factor (HIF) family of transcription factors. Neoangiogenesis in part alleviates growth-induced hypoxia but tumor vasculature lacks the normal hierarchical arrangement of artery–arteriole–capillary, resulting in intercellular gaps that leak, blood, and brains, and inefficient oxygen delivery. Consequently, within the growing mass, there are regions of hypoxia where certain cancer cells are deprived of oxygen. In response, tumor cells may undergo a metabolic shi causing acidosis. Hydrogen ($H^+$) ions generated by tumor cells during both aerobic and anaerobic glycolysis, glutaminolysis, and ATP hydrolysis are transported to the extracellular milieu creating an acidic tumor microenvironment. These acidic environments are thought to be permissive for tumor invasion and successive metastasis by inducing cell death in the surrounding normal tissue and degradation of the ECM. Parallel research also indicates that traditional 2D cell culture methods may not accurately mimic the 3D in vivo environment in which cancer cells reside (Figure 1), as the 2D environment does not allow for areas of hypoxia, heterogeneous cell populations (including stromal cells), varying cell proliferation zones (quiescent vs. replicating), ECM in uences, soluble signal gradients, and differential nutrient and metabolic waste transport6 (Figure 2). As a result, the unnatural 2D environment may provide inaccurate data regarding the predicted response of cancer cells

to chemotherapeutics7.

Cancer is a complex disease in which the cancer cell population dynamically evolves and the diversity of heterotypic interactions between cancer cells, surrounding cells, and environmental factors is spatiotemporally regulated. Therefore, preclinical models that incorporate factors that play critical roles in the dynamic tumor progression, within a biomimetic landscape are needed. Three-dimensional culture models help to deconstruct the complexity of cancer. Model systems can be engineered to recapitulate tumor cell-surrounding cell interactions, the physicochemical characteristics in an abiotic tumor environment, and the malignant transitions in tumor progression. They can provide insight into the evolutionary and ecological aspects of tumor progression, with relevant therapeutic implications.

Despite their great benefits over 2D models, 3D tissue models still encounter several limitations. One of their limitations lies in the requirement of large numbers of cells and cell types integrated into complex configurations. Second, ECM-derived matrices may have batch-to- batch variability in their biological characteristics. Some studies using standardized micro- fluidics- or microarray-based HTS for drug discovery or toxicity testing reported that specific ECM components or natural scaffolds were often not consistent. Third, 3D culture is generally very expensive for large-scale studies and high-throughput assays. Fourth, vascularization in 3D models remains an unsolved problem but it is the subject of active research, which plays a vital role in tissue growth and survival, and drug delivery. The core of tissue spheroids may create a hypoxic environment or limit

the diffusion of compounds into the core. These shortcomings are mainly due to a low level of biomimetic organization of the heterocellular environment, and instability and low repeatability of the developed 3D models. Biomimetically developed miniaturized tissue models that meet these limitations, by contrast, may be fabricated by the accurate deposition of cells and ECM components to recapitulate the native architecture of tissues, which is highly feasible using 3D bioprinting. Examples to specific capabilities of bioprinting will be further discussed in the next section.

The growth substrate is different, for 2D cell monolayer, it is rigid and insert, while 3D microtissues can mimic natural tissue environment. For, architecture, 2D cell monolayer is not physiological and cells partially interact while 3D structure is 'physiological', it can promote close interactions between cells and they have extracellular matrix(ECMs) as well as growth factors. There is no cell encapsulation in 2D cell monolayer. As for 2D cell monolayer, the growth factor diffusion is rapid, but for 3D microtissues, it is slow and biochemical gradients regulate cell-cell communication and signaling. ECM-based growth substrates provide a physiological environment that supports and promotes key cell functions, ECM molecules interact with cell surface receptors (e.g., regulation of integrin signaling by fibronectin: integrin interactions), also ECM appears to function in the storage and presentation of growth factors. Invasion and metastasis are responsible for approximately 90% of deaths caused by cancer. Metastasis is a highly complicated phenomenon that is associated with many different types of cells, connective tissues, and blood vessel components within different organs. Better understanding of cancer invasion and metastasis is key to the development of effective cancer intervention methods

including anticancer drugs. Well-defined tissue models, instead of more complicated in vivo models, would be ideal to perform systematic studies, particularly during the early development stages. However, most cancer models that are currently available fail to faithfully mimic cancer environments. Several studies have focused on better mimicking cancer environments and understanding the processes of cancer invasion and metastasis. Invasive and metastatic tumors are known to be heterogeneous as they contain a variety of subpopulations of cells with different metastatic potentials. Cellular heterogeneity in cancer tissues has been reported in epithelial cells. Moreover, a study on mammalian carcinoma showed greater differentiation of neoplastic stem cells compared to that in analogous noncancer tissues resulting in tumor heterogeneity. In addition, another study reported that stem cell biology could provide new insight into cancer biology. This study also proposes that tumors may contain a considerable amount of cancer stem cells.5 This is direct evidence that the behavior and fate of cancer cells rely on the tumor microenvironment (TME). Martin et al. also showed that mesenchymal stem cells (MSCs) have an influence on cell growth and metastasis through the regulation of epithelial-to-mesenchymal transition (EMT)-associated genes.

Materials. hASCs and MDA-MB-231 were obtained from Cefobio (Seoul, Korea) and American Type Culture Collection (Manassas, VA, USA), respectively. Rat tail collagen I used in this study was purchased from Corning (Corning, NY, USA). The Live–Dead Cell Staining Kit was purchased from BioVision (Seoul, Korea), and all antibodies used for immunofluorescence assays were obtained from Abcam (Cam- bridge, U.K.).

Cell Culture. hASCs (passage 6) were cultured under 5% CO2 atmosphere at 37 °C by using an hASC growth medium (Cefobio, Korea) containing supplement and 1% penicillin/ streptomycin. The medium was replaced every 3 days. MDA- MB-231 was maintained in RPMI 1640 medium supplemented with 10% fetal bovine serum (FBS) and 1% penicillin/ streptomycin. The medium was replaced every 2 days.

Preparation of the MBP-FGF2 Surface. The MBP-FGF2 surfaces were prepared using our previously published protocol.21,23 Briefly, MBP-FGF2 fusion protein was obtained from Escherichia coli carrying pMAL-FGF2 plasmids that were generated by the insertion of human FGF2 complement DNA (cDNA) (Bioneer, Korea) into the pMAL vector (New England Biolabs, U.K.). Human FGF2 165 cDNA was cloned from human fibroblasts by means of polymerase chain reaction (PCR) using oligonucleotide pairs (Bioneer; 5′ -CCGAA- TTCCCCGCCTTGCCCGAGGATGGC-3 ′ and 5 ′ -CAAAG-CTTTCAGCTCTTAGCAGACATTGGAAG-3 ′ ) including EcoR I and Hind III restriction sites, respectively. The PCR products were cloned into plasmid pGEM-T (Promega, USA) to generate pGEM-FGF2. The pGEM-FGF2 and plasmid pMAL were digested using EcoRI-Hind III and recovered from an agarose gel. The digested fragments were ligated using a ligation kit (Takara, Japan) to generate pMAL-FGF2. MBP- FGF2 (20 μg/mL) was spontaneously adsorbed to a polystyrene (PS) surface plates (nontissue culture-treated plate, 96- or 384-well plates; Falcon, Fisher Scientific, USA) at 37 °C for 4 h.21,22,24

Preparation of Clusters A and AC. hASCs or hASCs/ MDA-MB-231 suspensions were seeded on a MBP-FGF2- coated 96- or 384-well PS plate in the hASC growth medium (Cefobio, Korea). The medium was supplemented and cultured for 1 day in an incubator at 37 °C. After 24 h of culture, clusters A and AC were observed using an Axio Vert.A1 inverted microscope (Zeiss, Germany).

Viability and Morphology. For the live–dead cell assay, after 24 h, clusters A and AC were stained using the Live–Dead Cell Staining Kit (BioVision, Korea) for 1 h according to the manufacturer's protocol. After washing with PBS, the clusters were fixed in a formaldehyde solution and embedded into the optimal cutting temperature (O.C.T.) compound (SAKURA Tissue-Tek, USA) for 12 h and then frozen. The frozen clusters were sectioned into 10 μm thick samples at −20 °C and attached to glass slides. Clusters A and AC were encapsulated in collagen gels prepared using Rat tail collagen I at concentrations of 2, 4, and 6 mg/mL and fixed in a formaldehyde solution. The fixed gels were then embedded into the O.C.T. compound for 12 h and frozen. The frozen gel samples were sectioned into 10 μm thick sections at −20 °C and attached to the glass slides. The behaviors of clusters A and AC within the collagen gels were monitored using the Axio Observer microscope (Zeiss, Germany) over incubation of 0, 6, 12, 24, and 48 h. Prior to cluster formation, PKH67 labeled hASCs (PKH67 Green Fluorescent Cell Linker Mini Kit, Sigma, USA) and PKH26 labeled MDA-MB-231 (PKH26 Red Fluorescent Cell Linker Mini Kit, Sigma, USA) were seeded on a MBP-FGF2-coated 384-well PS plate in the hASC growth medium (Cefobio, Korea). At each of the concentrations of collagen gels

and the incubation hours, cell migration was defined by the distance the cells traveled from the center of the clusters measured using ImageJ software.

Scanning Electron Microscopy. The scanning electron microscope (SEM) images of clusters A and AC were obtained after formation of the clusters. After washing with PBS, the clusters were fixed in 2.5% glutaraldehyde solution at 4 °C for 30 min. The fixed clusters were maintained in the 2% osmium tetroxide ($OSO_4$) for 2 h at 4 °C, and washed with deionized water. After dehydration with dilute ethanol, the clusters were dried by evaporation using hexamethyldisilazane (HMDS) and stored in a vacuum chamber for 1 day before the imaging experiments. SEM images were then acquired using FE-SEM Hitachi S 4100 (Hitachi, Japan).

Immunofluorescence Staining. For the immunofluor- escence study to measure expression levels of CD44, fibronectin, α-SMA, and CXCR4, sections of clusters A- and AC-injected collagen gels were incubated at 4 °C with the corresponding primary antibodies (Abcam, U.K.). After washing the sections with PBS, antibody staining was performed using secondary antibodies (Abcam, U.K.) according to the manufacturer's protocol. Then, the sections were incubated with 4′,6′-diamidino-2-phenyl indole (DAPI) (Thermo Fisher Scientific, USA) for nucleus staining followed by actin staining using rhodamine phalloidin (Thermo Fisher Scientific, USA). The fluorescently labeled cells were finally observed under a LSM 700 laser scanning confocal microscope (Zeiss, Germany).

Statistical Analysis. Quantitative data were expressed as mean ± standard error of the mean

(SE). The significance of differences in the mean values was evaluated using the one-way ANOVA with Tukey tests. Differences were considered significant when the p value was less than 0.05 (marked as *). hown in Figure 1. For cluster AC, suspension of MDA-MB-231 cells and hASCs were cultured on the MBP-FGF2-coated PS plate. There were numerous approaches of forming spheroid clusters, such as culturing cells in nonstick U-bottom wells, in hanging drop, in rotating wall vessels, etc. Some reports have been shown that MDA-MB-231s were aggregated Matrigel or solid-like gel such as methylcellulose (MethoCel), DEX-in-PEG ATPS, and poly-HEMA.25–29 On the poly- HEMA coated plates, MDA-MB-231 form loose aggregates of cells after 24 h. The cell–cell interactions established by this method are weak, and the aggregates can be easily regressed mechanically by pipetting without additives such as collagen and reconstituted basement membrane. MDA-MB-231 cells did not form clusters because these epithelial cells do not produce ECMs in our systems (Figure S1). In a similar manner, we believe the reason why MDA-MB-231 does not form a stable cell cluster is because an interaction force between the cells is much weaker than that between cell and the surface coated with MBP-FGF2, the membrane binding motif. Thus, we used our 3D cluster model to permit rapid experimental manipulations, testing of hypotheses, and reducing nonuniformity. This method allows an efficient formation of 3D coculture model of stromal cells and epithelial cells, offering a uniform cluster formation with various sizes, strengths, and cell populations that are distinct from other methods (Figure S2).

After 24 h, the morphology of clusters A and AC were observed in a 384-well PS plate

using phase contrast microscopy (Figure 2a). Live–dead cell assays of clusters A and AC using confocal microscopy differentiate live and dead cells, appearing as green and red colors, respectively (Figure 2b). After 24 h, both clusters A and AC showed healthy cells but with different roughness of the edges. Cluster AC had rougher surface morphology than cluster A. Figure 2c shows the SEM images of clusters A and AC, revealing that hASCs in cluster A are associated and interlinked with the ECM fibers (white arrow) surrounding the cell membrane surfaces. In contrast, cluster AC did not show the ECM fibers. This result indicates different cell-ECM-cell interactions in cluster AC from that in cluster A during the cluster formation. Collective cell behaviors are defined as an orchestrated movement among interconnected cell groups.30 It is exploited by cancer cells as an efficient invasion strategy that can be modeled in the laboratory.31 The ECM remodeling surrounding the cells, resulting in a topological rearrangement of ECM fibers that in turn shape the tissue microenvironment or promote invasive phenotypes.32 The formation of ECM fiber might be improved by their biophysical interaction of the cell-ECM-cell contact and cell-matrix adhesion, as illustrated in Figure 1a, which is not the case for cluster AC.

Behaviors of Clusters A and AC within Collagen Gels.

In the body, stiffness of a 3D matrix is an important factor for the growth and differentiation of cells.2,33 In addition, microenvironments can regulate cell function and tissue integrity, including migration and alterations in cell-to-cell and cell-matrix adhesions. The elasticity and stiffness of tissues have been reported to be linked to cancer biology.34,35 For

example, cancer progression in soft tissues is correlated with an increase in stiffness due to local accumulation, often caused by cross-linked collagen matrices of the tumor via physical interactions.

We prepared clusters A and AC within collagen gels with different matrix densities.36 To study different matrices that mimic in vivo systems, collagen concentrations of 2, 4, and 6 mg/mL were used for this study. The storage modulus (G′) of collagen gel at 25 °C prepared from the collagen solutions carried over 300–500, 800–1800, and 2300–4700 Pa at concentration of 2, 4, and 6 mg/mL, respectively (Figure S3).

The morphological changes of clusters A and AC within the collagen gels were monitored using live cell microscopy (Figure 3a and Video S1). A time-lapse video shows different movement patterns of cell migration from clusters A and AC. Additionally, the fluorescence images of the cells after staining with green and red dyes for hASCs and MDA-MB-231, respectively, indicate that both cells do migrate (Figure 3b). During cell migration, hASCs (black arrow) showed the fibroblast-like escaping behavior from cluster A. However, behaviors of MDA-MB-231 (white arrow) appeared to be drastically different from those of hASCs. Cell migration was measured at 20 spots, as defined by distances from the center of the clusters after 48 h (Figure 3c). This data shows that the concentration of the collagen gels, although modest, affects cell

ECM remodeling surrounding the cells, resulting in a topological rearrangement of ECM

fibers that in turn shape the tissue microenvironment or promote invasive phenotypes. The formation of ECM fiber might be improved by their biophysical interaction of the cell-ECM-cell contact and cell-matrix adhesion. In the body, stiffness of a 3D matrix is an important factor for the growth and differentiation of cells. In addition, microenvironments can regulate cell function and tissue integrity, including migration and alterations in cell-to-cell and cell-matrix adhesions. The elasticity and stiffness of tissues have been reported to be linked to cancer biology. For example, cancer progression in soft tissues is correlated with an increase in stiffness due to local accumulation, often caused by cross-linked collagen matrices of the tumor via physical interactions. The cells showed fast movement in stiff hydrogels because the increased stiffness of the gels simultaneously increased the adhesion site density of compounds such as integrin. In addition, integrin receptors and fibronectin appear to play important roles in migration and invasion.

Fig. 3G and H show a similar distribution in cell number- uorescent intensity plots of both samples: 72.3% cells with internalized nanoparticles and 71.9% cells without internalized nanoparticles are in G0/G1, suggest- ing that internalization does not change cell cycles. Fig. 5A and B show ow cytometry results of X-ray irradiated cells with negatively charged nanoparticles and internalized nanoparticles, respectively. 38.8% cells with nega- tively charged nanoparticles and 72.4% cells with internalized nanoparticles show a uorescence intensity below 1 unit, sug- gesting that internalized nanoparticles can enhance X-ray induced DNA damage. Fig. 5C shows the MFI of each sample: cells with negatively charged nanoparticles (1.38 106), cells with internalized nanoparticles

alone (1.38 106), cells with negatively charged nanoparticles and X-ray (1.25 106), and cells with internalized nanoparticles and X-ray (0.82 106). Cell death (apoptosis) a er different treatments has also been determined using ow cytometry. A speci c number of cells (106) with internalized positively charged nanoparticles are exposed to X-ray irradiation for different times, and cultured in medium for 48 h. Dead cells that oat up in medium are collected, enriched by centrifugation, stained with PI, and counted by ow cytometry. As the irradiation time increases from 0, 1, 5, to 15 min, more cells are killed (Fig. 5D). Cells with negatively charged nanoparticles and X-ray are tested as comparison, where fewer cells are killed even when radiation conditions are the same

X-ray photons in radiation therapy can generate photoelectrons and Auger electrons, which can cause ionization of water and formation of reactive free radicals (mostly hydroxyl radicals). The free radicals diffuse through chain reactions in cells, and damage DNA in mitochondria and nuclei by extracting hydrogen atoms from ribose sugars, leading to cleavage of the polynucleotide backbone. A challenge of X-ray radiation therapy is that high dose X-ray can damage normal cells and cause side effects due to its low tumor selectivity. Nanoparticles of gold, platinum or bismuth have been proposed to enhance radiation therapy, but the measured effect of nanoparticles is negligible. This is likely due to the fact that these nanoparticles are attached on the cell membrane, and X-ray generated free radicals have to diffuse into the vicinity of DNA to cause damage. If

radiosensitizers could be placed in cancer cells or nuclei, the amount of free radicals available for DNA damage will be enhanced, and the total X-ray dose could be reduced to receive the same treatment effect.

Figure 3. (a) Morphological change of clusters A and AC in collagen gel as a function of concentration (2, 4, and 6 mg/mL) at 48 h. The dashed line indicates initial cluster shape. The black and white arrow indicates migrated hASCs and cancer cells. (b) Fluorescence images of clusters A and AC in collagen gel (2, 4, and 6 mg/mL) at 48 h. The inset shows a higher magnified view. The hASCs (green arrow) and MDA-MB-231 (red arrow) stained with PKH67 and PKH27, respectively. The scale bar is 500 μm. (c) Migrated distances (μm) comparison of clusters A and AC in collagen gel (2, 4, and 6 mg/mL) at 48 h. The distance of migrating cells was measured by ImageJ software (mean ± SE, n = 20; ANOVA, $p < 0.05$; * vs 2 mg/mL).

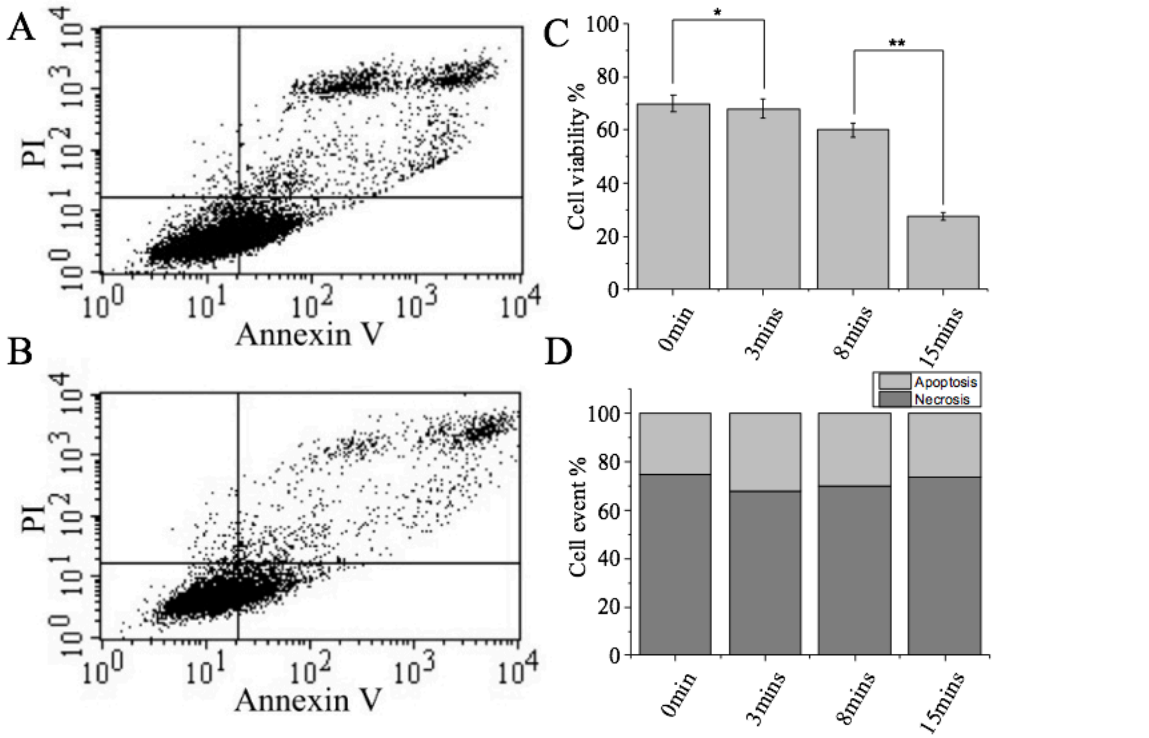
A
B
C
D
PI
Annexin V
Cell viability %
Cell event %
Apoptosis
Necrosis
0min
3mins
8mins
15mins

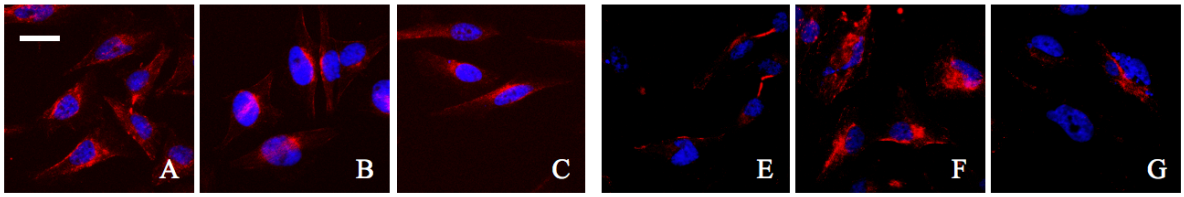
A
B
C
E
F
G

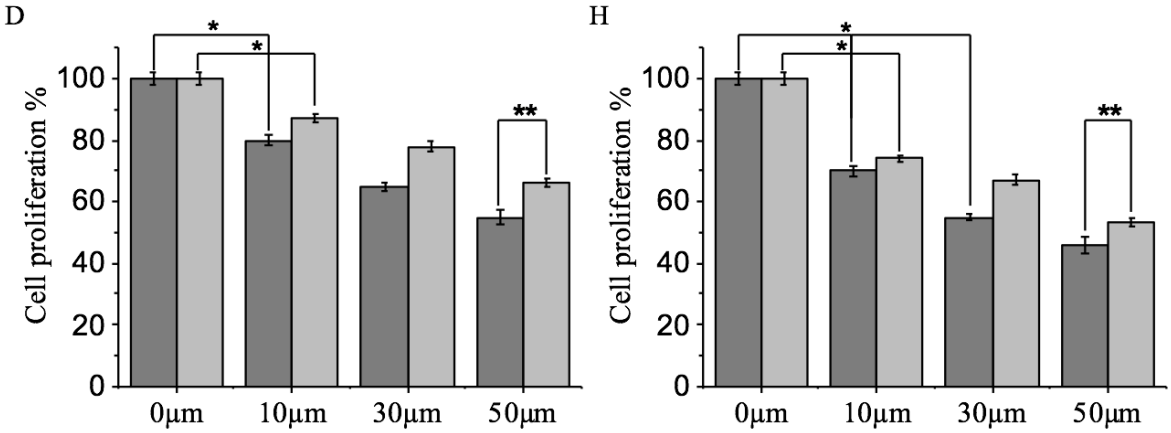
D
H
Cell proliferation %
0μm
10μm
30μm
50μm

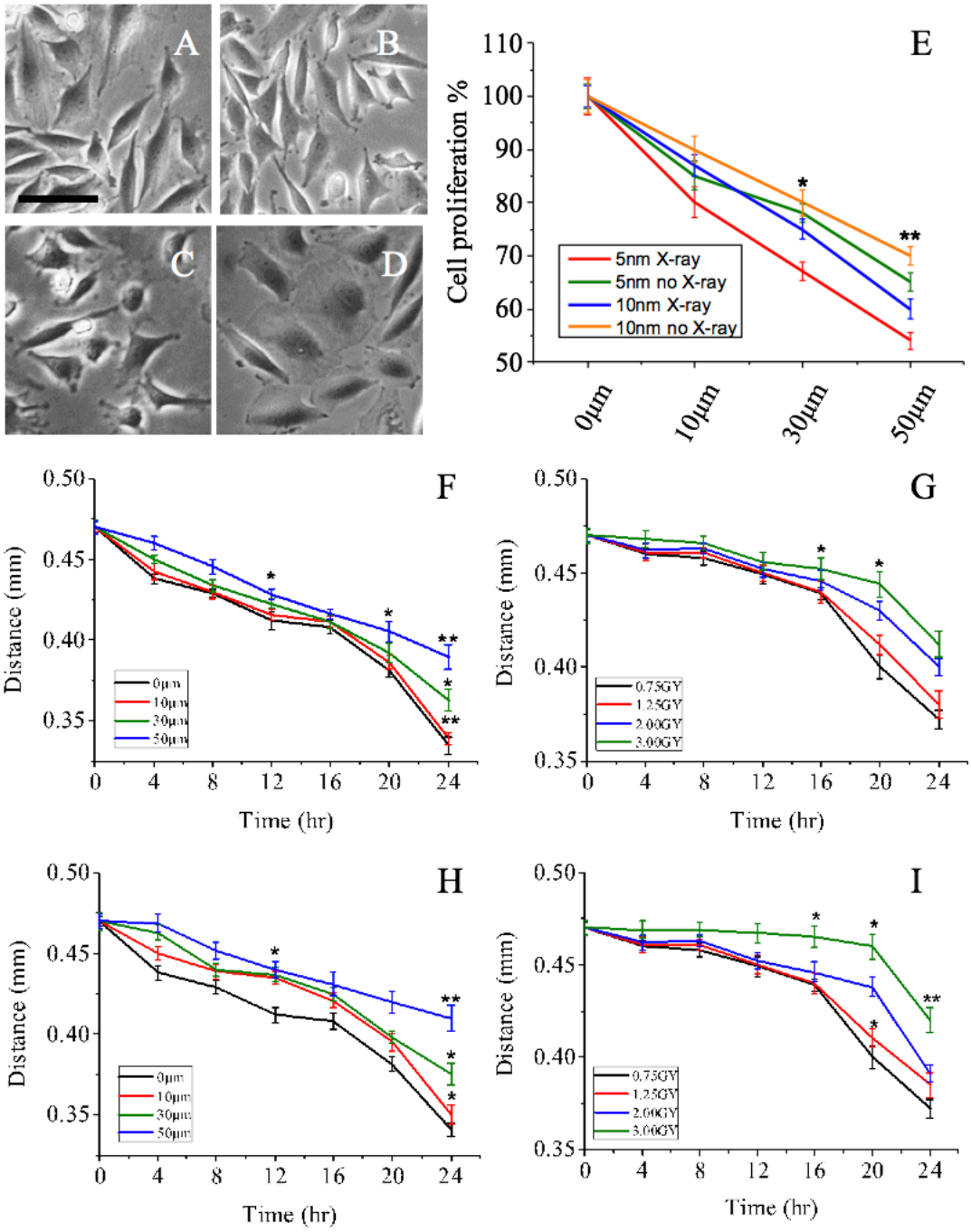
A
B
C
D
E
Cell proliferation %
110
100
90
80
70
60
50
5nm X-ray
5nm no X-ray
10nm X-ray
10nm no X-ray
0μm
10μm
30μm
50μm
F
Distance (mm)
0.50
0.45
0.40
0.35
0
4
8
12
16
20
24
Time (hr)
G
0.75GY
1.25GY
2.00GY
3.00GY
H
I

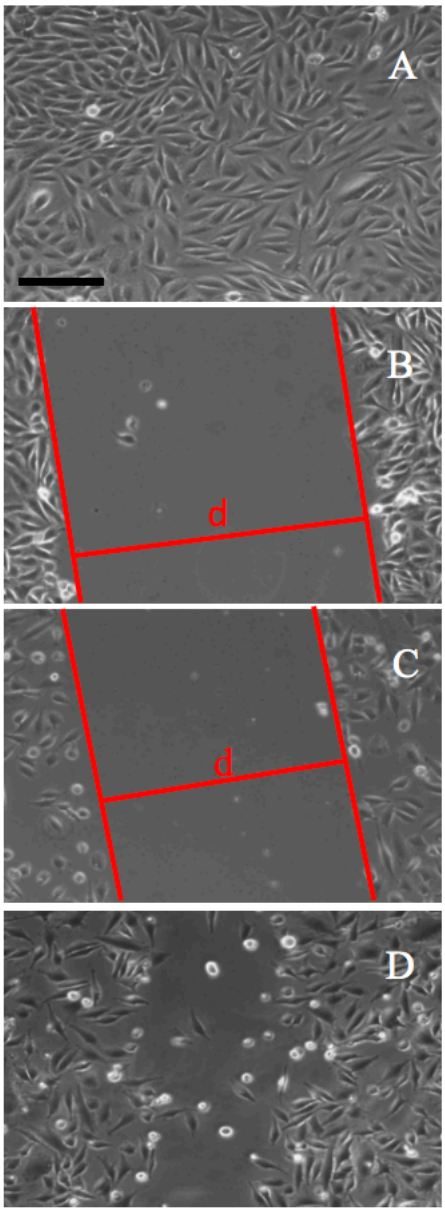
A
B
d
C
d
D

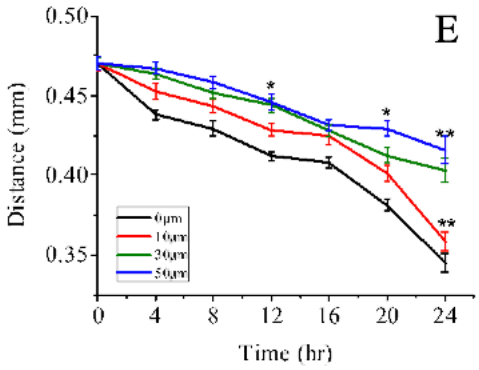
E
Distance (mm)
0.50
0.45
0.40
0.35
0
4
8
12
16
20
24
Time (hr)
*
*
**
**
0μm
16μm
30μm
50μm

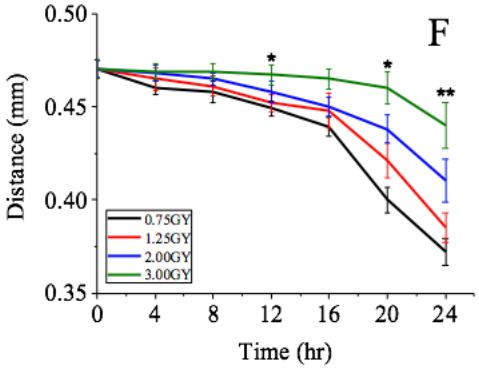
F
Distance (mm)
0.50
0.45
0.40
0.35
0
4
8
12
16
20
24
Time (hr)
*
*
**
0.75GY
1.25GY
2.00GY
3.00GY

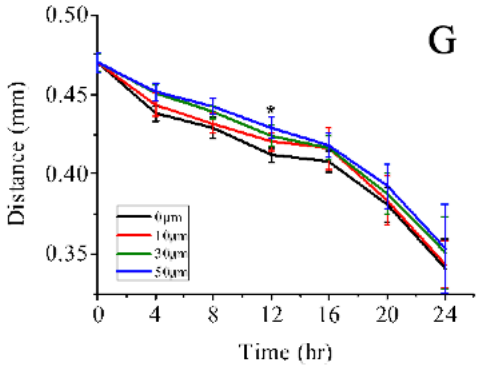
G
Distance (mm)
0.50
0.45
0.40
0.35
0
4
8
12
16
20
24
Time (hr)
*
0μm
16μm
30μm
50μm

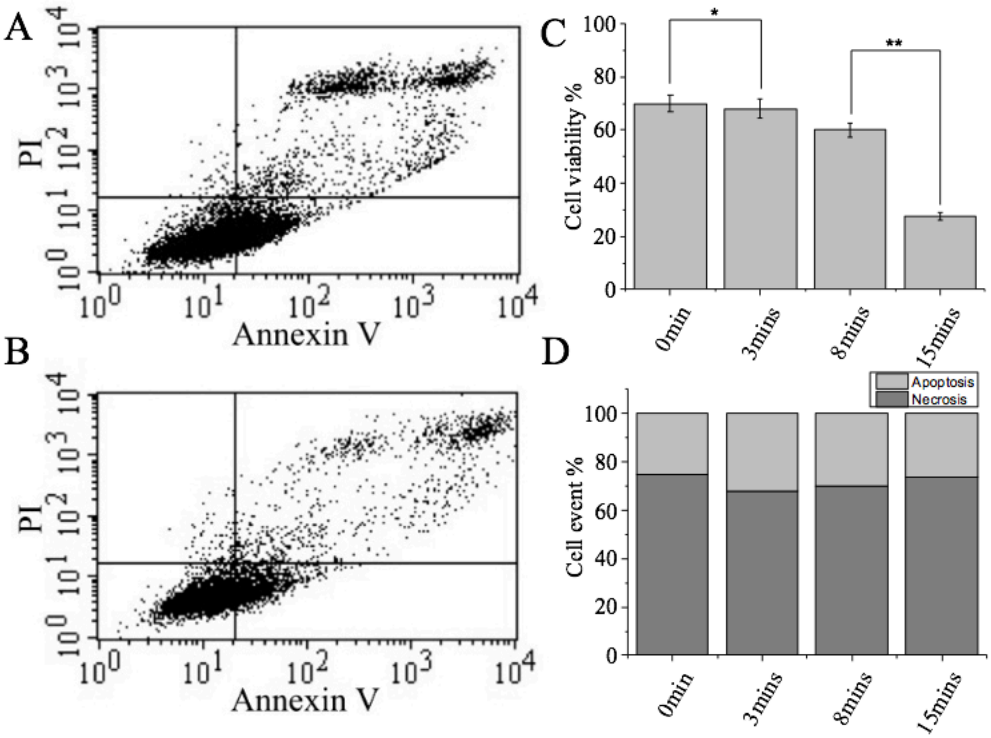
A
B
C
D
PI
Annexin V
Cell viability %
Cell event %
0min
3mins
8mins
15mins
Apoptosis
Necrosis
*
**

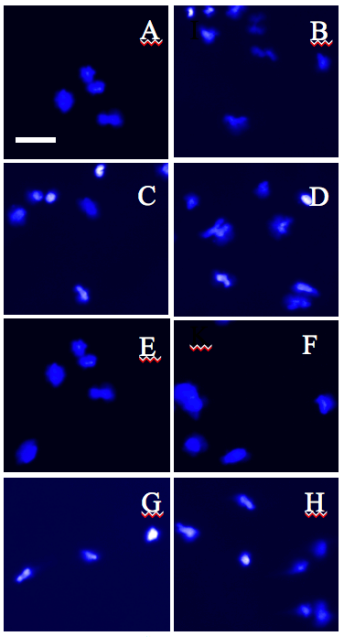
A
B
C
D
E
F
G
H

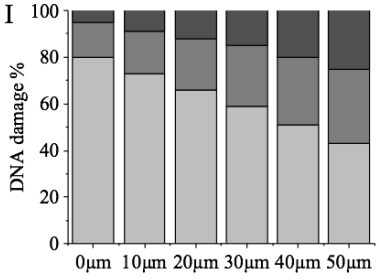
I
DNA damage %
100
80
60
40
20
0
0μm 10μm 20μm 30μm 40μm 50μm

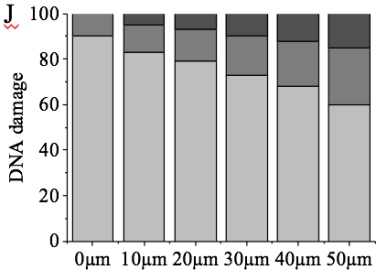
J
DNA damage
100
80
60
40
20
0
0μm 10μm 20μm 30μm 40μm 50μm

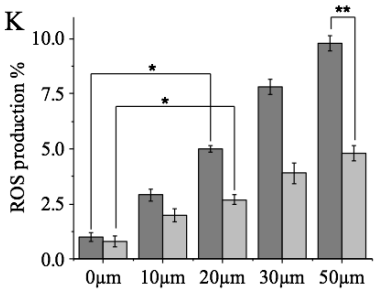
K
ROS production %
10.0
7.5
5.0
2.5
0.0
*
*
**
0μm 10μm 20μm 30μm 50μm

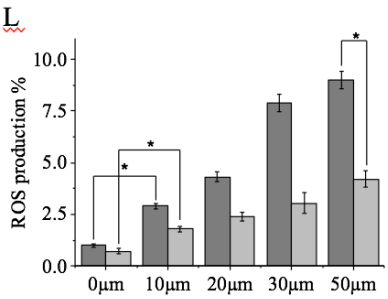
L
ROS production %
10.0
7.5
5.0
2.5
0.0
*
*
*
0μm 10μm 20μm 30μm 50μm

(a)

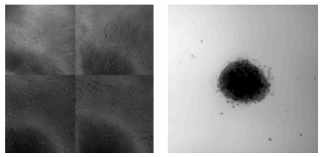

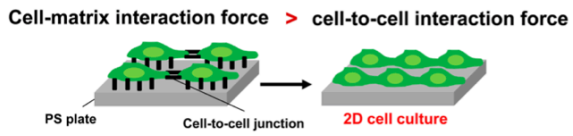
Cell-matrix interaction force > cell-to-cell interaction force
PS plate
Cell-to-cell junction
2D cell culture

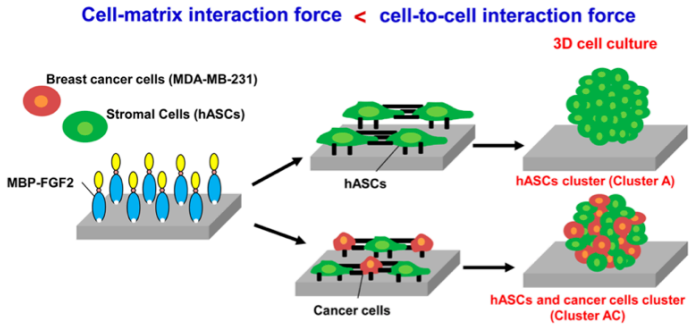
Cell-matrix interaction force < cell-to-cell interaction force
3D cell culture
Breast cancer cells (MDA-MB-231)
Stromal Cells (hASCs)
MBP-FGF2
hASCs
hASCs cluster (Cluster A)
Cancer cells
hASCs and cancer cells cluster
(Cluster AC)

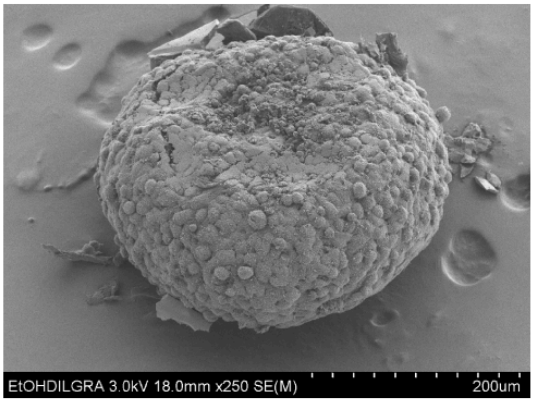
EtOHDILGRA 3.0kV 18.0mm x250 SE(M)
200um

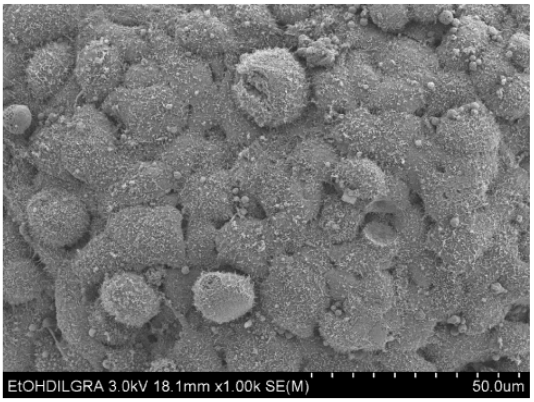
EtOHDILGRA 3.0kV 18.1mm x1.00k SE(M)
50.0um

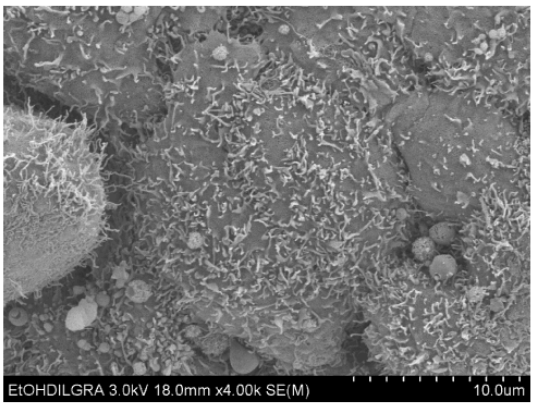
EtOHDILGRA 3.0kV 18.0mm x4.00k SE(M)
10.0um

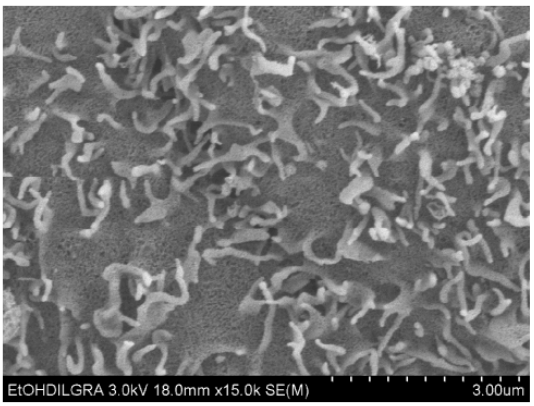
EtOHDILGRA 3.0kV 18.0mm x15.0k SE(M)
3.00um

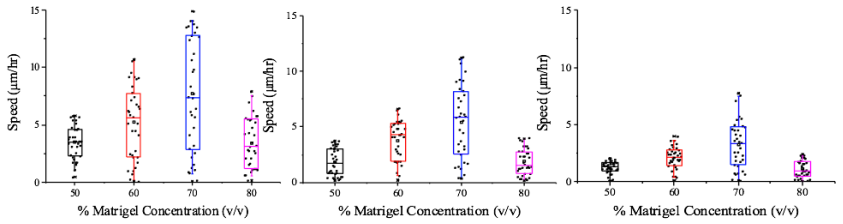
Speed (μm/hr)
% Matrigel Concentration (v/v)

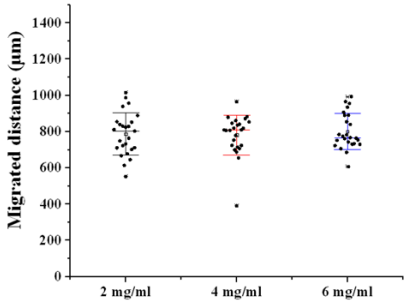
Migrated distance (μm)
2 mg/ml
4 mg/ml
6 mg/ml

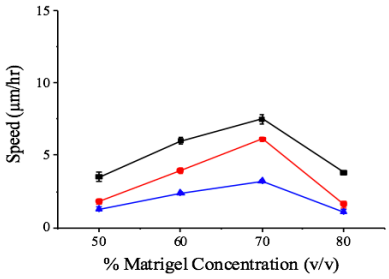
Speed (μm/hr)
% Matrigel Concentration (v/v)

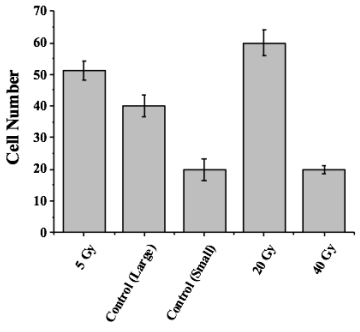
Cell Number
5 Gy
Control (Large)
Control (Small)
20 Gy
40 Gy

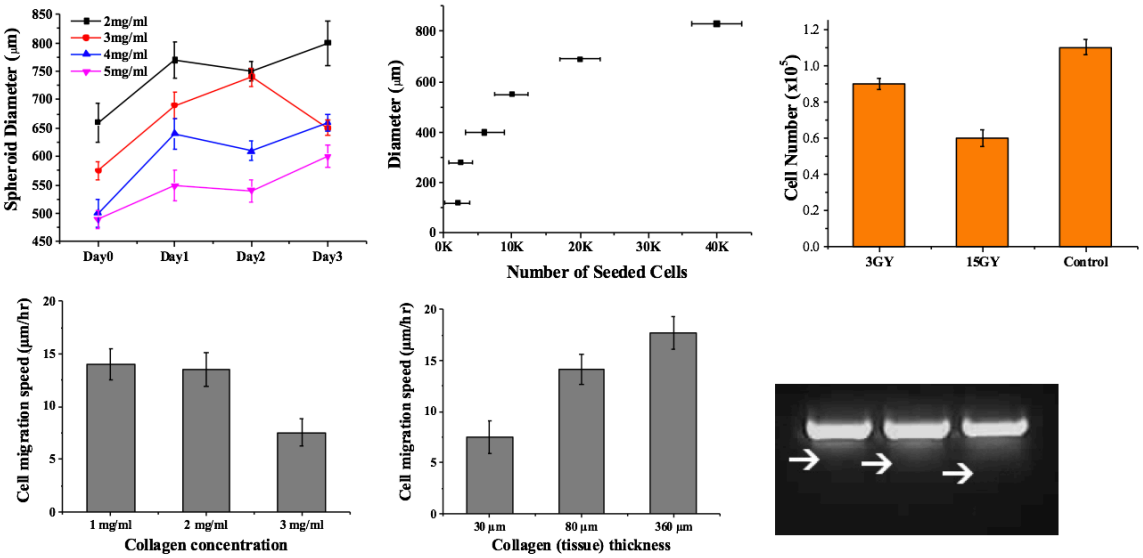
Spheroid Diameter (μm)
2mg/ml
3mg/ml
4mg/ml
5mg/ml
Day0
Day1
Day2
Day3
Diameter (μm)
Number of Seeded Cells
Cell Number (x10^5)
3GY
15GY
Control
Cell migration speed (μm/hr)
1 mg/ml
2 mg/ml
3 mg/ml
Collagen concentration
Cell migration speed (μm/hr)
30 μm
80 μm
360 μm
Collagen (tissue) thickness

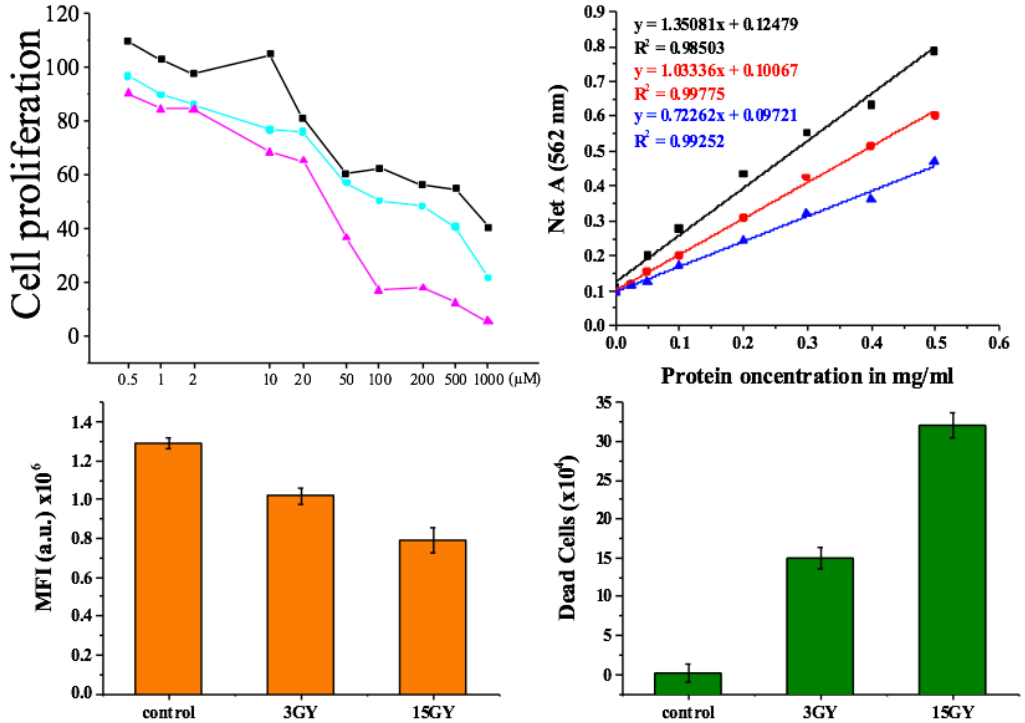
Cell proliferation
0.5
1
2
10
20
50
100
200
500
1000 (μM)
y = 1.35081x + 0.12479
R² = 0.98503
y = 1.03336x + 0.10067
R² = 0.99775
y = 0.72262x + 0.09721
R² = 0.99252
Net A (562 nm)
Protein oncentration in mg/ml
MFI (a.u.) x10^6
control
3GY
15GY
Dead Cells (x10^4)
control
3GY
15GY

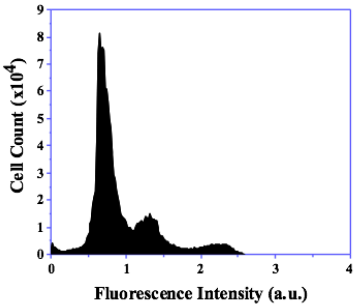
Cell Count (x10^4)
Fluorescence Intensity (a.u.)

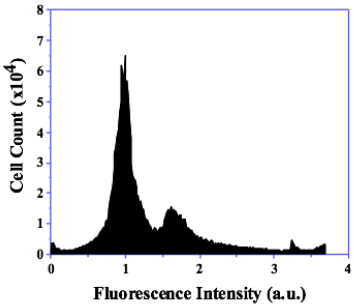
Cell Count (x10^4)
Fluorescence Intensity (a.u.)

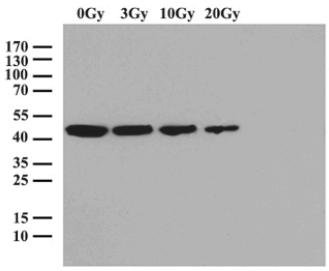
0Gy 3Gy 10Gy 20Gy
170
130
100
70
55
40
35
25
15
10

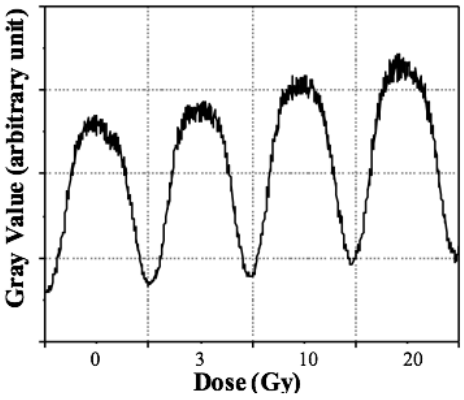
Gray Value (arbitrary unit)
0
3
10
20
Dose (Gy)

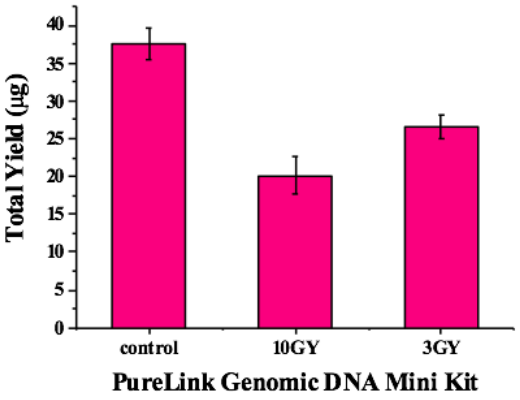
Total Yield (μg)
control
10GY
3GY
PureLink Genomic DNA Mini Kit

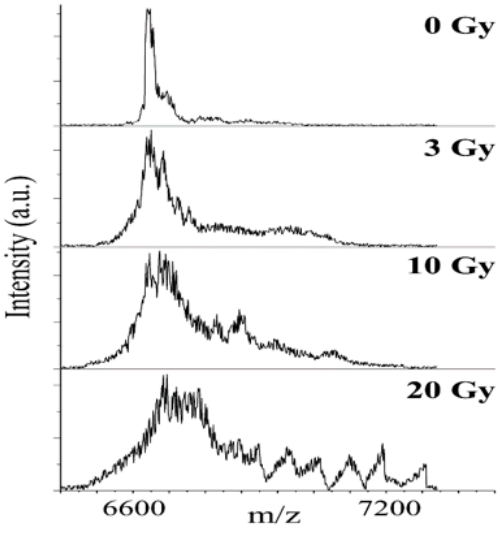
0 Gy
3 Gy
10 Gy
20 Gy
Intensity (a.u.)
6600
m/z
7200